PAPER

Enzyme-sensitive magnetic core–shell nanocomposites for triggered drug release†

Chunyu Yang,[a] Wei Guo,[b] Na An,[a] Liru Cui,[a] Ting Zhang,[a] Ruihan Tong,[a] Yuhua Chen,[a] Huiming Lin[*a] and Fengyu Qu[*a]

Fe_3O_4@$mSiO_2$ (magnetic Fe_3O_4 core coated by a mesoporous silica shell) nanoparticles were successfully synthesized as a carrier. The anti-cancer drug doxorubicin (DOX) and chlorambucil (Chl) were used as the model cargo. After the drug-loading, a sodium hyaluronic acid (HA) cross-linked gel was adopted to coat the outside of the Fe_3O_4@$mSiO_2$ nanoparticles as a layer (named as drug–Fe_3O_4@$mSiO_2$–HA) to prevent drug pervasion. The detailed release kinetics were investigated, revealing the sensitive release triggered by hyaluronidase (HAase), a major enzyme which is rich in the tumor microenvironment, which can degrade the HA shell to induce the enzyme sensitive drug release. Moreover, there are some HA receptors in many tumor areas, associating with magnetic targets to further ensure the specific targeted drug delivery. With these improved performances, these smart multifunctional nanocomposites are expected to possess potential applications in the biopharmaceutical for cancer therapy.

Introduction

Cancer has become a serious disease to human health and life.[1] To date, tens of millions of people worldwide have suffered from various forms of cancers. Currently, radiation,[2] surgery,[3] and chemotherapy[4] are used to treat these malignant tumors, but chemotherapy remains one of the most frequent treatments for many cancers. However, chemotherapy always induces huge side effects besides the efficacy, originating from the inherent cytotoxicity and the little specific discrimination between normal cells and cancer cells.[5] With the continuous development of nanotechnology, researchers have focused on the preparation of drug delivery systems (DDSs) to improve the targeting drug efficacy as well as the anti-cancer therapy effect.[6–9] In DDSs, mesoporous silica nanoparticles (MSNs) have been widely applied as drug carrier because of their flexible and robust properties, including excellent chemical stability, easily modification, and outstanding biocompatibility.[10–12] Meanwhile, MSNs nanoparticles also can endow different structures with a variety of attractive features, including very high pore volume, large surface area, low density, tunable pore size, and high loading capacity.[13–15] However, based on previous reports, pure MSNs materials always reveal many prematurity and poor targeting performance. To address this dilemma, functionalized MSNs have attracted a lot of attention for targeted drug release toward a specific region by introducing other controlled factors.[16,17] To prevent premature drug release before reaching the target cells is to use stimuli-responsive systems with controlled release features in response to a given stimulus, such as magnetic,[18] temperature,[19] electricity,[20] redox activation,[21] enzymatic activity,[22] and pH.[23] For instance, Zhao and co-workers constructed a novel pH-sensitive with β-cyclodextrin (β-CD) positioned on the surface of mesoporous silica and demonstrated that pH-triggered cargo release under acid pH conditions.[24]

Magnetic iron oxide nanoparticles (Fe_3O_4) with strong magnetic property and low toxicity have been approved as safe nanomaterials for their potential applications in a variety of biomedical fields, including magnetically guided drug deliver, hyperthermia treatment, cell separation, and magnetic resonance imaging (MRI), and so forth.[25–27] However, pure Fe_3O_4 is prone to aggregation due to anisotropic dipolar attraction and rapid biodegradation when they are exposed to biological systems directly.[28,29] The core–shell structure with Fe_3O_4 nanoparticles as core and mesoporous silica as shell not only can overcome the limitation compare to pure Fe_3O_4 nanoparticles but also can combine the advantages of the two to improve the performance in the field of targeted drug delivery.[30,31]

Under this concept, we developed a new nanoplatform, revealing the targeting and enzyme-sensitive drug delivery behavior. As illustrated in Scheme 1, Fe_3O_4@$mSiO_2$ nanoparticles were firstly prepared as the nanocarrier with Fe_3O_4 as core and mesoporous silica as shell. Then, doxorubicin (DOX) and chlorambucil (Chl) were utilized as a model anti-cancer drug to illuminate the release kinetics. It is known that sodium

[a]College of Chemistry and Chemical Engineering, Harbin Normal University, Harbin 150025, P. R. China. E-mail: qufengyu@hrbnu.edu.cn; linhuiming@hrbnu.edu.cn; Tel: +86-451-88060653

[b]Key Laboratory of Microsystems and Microstructures Manufacturing, Ministry of Education, Harbin Institute of Technology, Harbin 150080, P. R. China
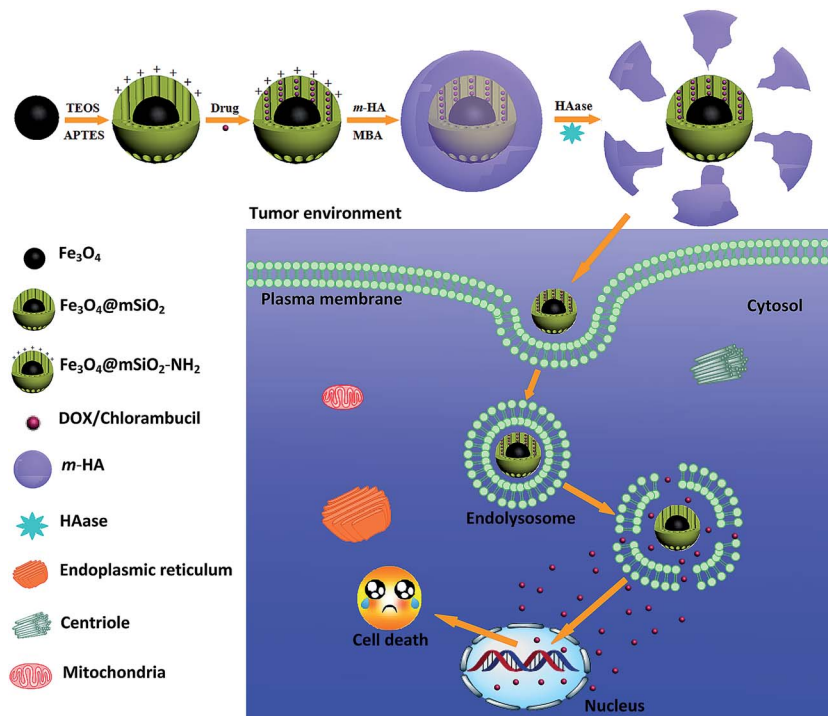
Scheme 1 Illustration of the preparation and controlled release process of drug−Fe$_3$O$_4$@mSiO$_2$−HA.

hyaluronic acid (HA) is biodegradable, biocompatible and non-immunogenic and can be readily degraded by hyaluronidase (HAase) which is the major enzyme to rich in the tumor microenvironment and the tumour cellular endocytic vesicles including endosomes and lysosomes (endolysosomes).[32–37] In addition, the specific interaction between HA and cancer cells overexpressing active tumour-targeting ligands to bind the receptors has recently received wide attention due to the HA receptors, such as cluster determinant 44 (CD44) and receptor for hyaluronan mediated motility (RHAMM), especially the CD44, which are overexpressed of several tumor cells than normal cells.[38–40] In particular, researchers focused on the use of HA as a targeting moiety for cancer therapy. Herein, HA was used to coat around Fe$_3$O$_4$@mSiO$_2$ nanoparticles by a typical photocrosslinking[36] reaction to block the pore and regulate the drug release. Thanks to the overexpressed HAase in the tumor microenvironment, the degradation of HA induce the sensitive drug release performance. In addition, the magnetic passive targeting associated with special recognition of HA may be expected to enhance the targeting behavior of the novel nano-vehicle to be used in biomedicine field.

Experiment and methods

Materials

Unless specified, all of the chemicals used were analytical grade and used without further purification. Tetraethyl orthosilicate (TEOS), cetyltrimethylammonium bromide (CTAB), 3-[4,5-dimethylthialzol-2-yl]-2,5-diphenyltetrazolium bromide (MTT), doxorubicin hydrochloride (DOX), (3-aminopropyl)triethoxysilane (APTES), 4′,6-diamidino-2-phenylindol, 2-(4-amidinophenyl)-1H-indole-6-carboxamidine, (DAPI dihydrochloride), 1-octadecene, sodium oleate, iron oleate, oleic acid, fluorescein isothiocyanate (FITC) were obtained from Aladdin, China. Ferric trichloride hexahydrate (FeCl$_3$·6H$_2$O), ethanol, chloroform, n-hexane were purchased from Tianjin Chemical Corp. of China. Sodium hyaluronic acid (HA, the molecular weight of 77 kDa) and hyaluronidase (HAase) was purchased from Freda Biochem Co., Ltd (Shandong, China). Chlorambucil (Chl) was purchased from J&K Scientific Ltd. N,N′-Methylenebisacrylamide (MBA) and Irgacure 2959 were purchased from Sigma-Aldrich.

Synthesis of iron oleate complex

In a typical synthesis of iron oleate complex, 10.8 g of iron chloride (FeCl$_3$·6H$_2$O, 40 mmol) and 36.5 g of sodium oleate (120 mmol, 95%) was dissolved in a mixture solvent composed of 80 mL ethanol, 60 mL distilled water and 140 mL n-hexane. The resulting solution was heated to 70 °C and kept at that temperature for 4 h. When the reaction was completed, the upper organic layer containing the iron oleate complex was washed three times with 30 mL distilled water in a separatory funnel. After washing, n-hexane was evaporated off, resulting in iron oleate complex in a waxy solid form.

Synthesis of Fe$_3$O$_4$ nanoparticles

Following a literature procedure,[41] Fe$_3$O$_4$ nanoparticles were prepared.[41] 36 g (40 mmol) of the iron oleate and 5.7 g of oleic acid (20 mmol, 90%) were dissolved in 200 g of 1-octadecene (90%) at room temperature. The reaction mixture was heated to 320 °C with a constant heating rate of 3.3 °C min^{-1}, and then

kept at that temperature for 30 min. When the reaction temperature reached 320 °C, a severe reaction occurred and the initial transparent solution became turbid and brownish black. The resulting solution containing the nanocrystals was then cooled to room temperature, and 500 mL of ethanol was added to the solution to precipitate the nanocrystals, which were further collected by centrifugation and then dispersed in chloroform.

Synthesis of Fe₃O₄@mSiO₂ nanoparticles

In a typical procedure, 0.5 mL of the Fe_3O_4 nanocrystals in chloroform (5 mg mL^{-1}) was washed with chloroform and collected by centrifugation at 8000 rpm for 10 min. Then the precipitate was poured into 4 mL of 0.2 M aqueous CTAB solution and the resulting solution was stirred vigorously for 30 min. The formation of an oil-in-water microemulsion resulted in a turbid brown solution. Then, the mixture was slowly heated up to 60 °C for to eliminate the chloroform, resulting in a transparent black Fe_3O_4/CTAB solution. To fully disperse the Fe_3O_4 nanoparticles, the solution was sonicated and stirred alternately. Then, 4 mL distilled water was added to the obtained black solution and the pH value of the mixture was adjusted to 8–9 by using 0.1 M NaOH. After that, 100 μL of 20% TEOS in ethanol was dropwise added three times at a 30 min intervals under vigorous stirring. The reaction mixture was reacted for 24 h at 32 °C under violent stirring. The as-synthesized Fe_3O_4@mSiO₂ NPs were centrifuged and rinsed with ethanol repeatedly to remove the excess precursors and CTAB molecules.

Synthesis of amino-functionalized Fe₃O₄@mSiO₂ (Fe₃O₄@mSiO₂–NH₂)

To functionalize the outer surface of Fe_3O_4@mSiO₂ with amino groups,[42] as-synthesized Fe_3O_4@mSiO₂ (300 mg) was suspended in dry toluene (20 mL) that contained APTES (100 μL). The solution was stirred at 50 °C under nitrogen for 4 h. The product was recovered by centrifugation and washed with ethanol and finally dried in a vacuum.

Drug loading

Typically, Fe_3O_4@mSiO₂–NH₂ (60 mg) and DOX/Chl (3 mg/30 mg) were added to the phosphate buffer solution/methanol (PBS; 3 mL, pH 7.4/5 mL) and stirred at 25 °C for 12 h/6 h, the drug-loaded mesoporous materials (named as drug–Fe_3O_4@mSiO₂–NH₂) were recovered by centrifugation and dried at room temperature under vacuum. To evaluate the drug-loading efficiency and encapsulation content, we determined the content of the residual drug in the supernatant by UV/Vis measurements at 480/256 nm. The loading efficiency (LE wt%) of drug can be calculated by using the formula (1). The experiment repeated three times.

$$LE\ wt\% = \frac{m_{(original\ drug)} - m_{(residual\ drug)}}{m_{(Fe_3O_4@mSiO_2-NH_2)} + m_{(original\ drug)} - m_{(residual\ drug)}} \times 100\% \quad (1)$$

Synthesis of FITC-labeled drug–Fe₃O₄@mSiO₂–NH₂

In a typical synthesis of FITC–APTES, 15 mg of FITC and 100 μL of APTES were dissolved in ethanol (5 mL) and the resulting solution was stirred at room temperature and kept in the dark for 24 h. FITC–APTES was attached to drug–Fe_3O_4@mSiO₂–NH₂ by reaction of the silica coupling groups of FITC–APTES and the residual Si–OH on the silica spheres. In a typical process, drug–Fe_3O_4@mSiO₂–NH₂ (60 mg) was dispersed, and then the obtained FITC–APTES solution (2 mL) was added. The reaction was performed in the dark at ambient temperature overnight. The solid was collected by centrifugation, followed by washing with deionized water and finally dried in a vacuum (for convenience, it is also denoted as the drug–Fe_3O_4@mSiO₂–NH₂).

Synthesis of methacrylated HA (m-HA)

HA was modified with double bond by reacting with the methacrylic anhydride (MA).[43] 1.0 g of HA was dissolved in 50 mL of distilled water with stirring in cold room overnight, followed by the addition of 0.8 mL of MA into the HA solution. The pH of the reaction was maintained between 8 and 9 by adding 5 M NaOH and kept at 4 °C under continuous stirring for 24 h. Then the product was collected and named m-HA. Subsequently, m-HA was precipitated in acetone, this solid crude product was filtered, washed with ethanol, and dried in air. The NMR spectrum of as-synthesized m-HA in D_2O is shown in Fig. S2.†

Synthesis of drug–Fe₃O₄@mSiO₂–HA

In a typical procedure, 3 mg of m-HA was dissolved in 20 mL of distilled water at room temperature. When it is completely dissolved, 200 μL of NaOH (0.1 M) and 0.15 g/0.10 g/0.05 g of drug–Fe_3O_4@mSiO₂–NH₂ were added and then kept at that temperature for 1 h, followed by adding a crosslinker, N,N'-methylenebisacrylamide (MBA) (MBA : m-HA = 1 : 1, w/w) and a photo-initiator Irgacure 2959 (0.1%, w/v). After radical polymerization via UV radiation for 2 min using a BlueWave 75 UV Curing Spot Lamp (DYMAX), drug–Fe_3O_4@mSiO₂–HA (for simplicity, DOX–Fe_3O_4@mSiO₂–HAs are denoted as the DOX–Fe_3O_4@mSiO₂–HA-1, DOX–Fe_3O_4@mSiO₂–HA-2, DOX–Fe_3O_4@mSiO₂–HA-3, Chl–Fe_3O_4@mSiO₂–HAs are denoted as the Chl–Fe_3O_4@mSiO₂–HA-1, Chl–Fe_3O_4@mSiO₂–HA-2, Chl–Fe_3O_4@mSiO₂–HA-3, respectively) was obtained by washing with distilled water using centrifugal filters to remove the excessive crosslinker and initiator.

Drug release

Gating protocol was investigated by studying the release profiles of drug from the drug–Fe_3O_4@mSiO₂–HA using a semipermeable dialysis-bag diffusion technique (molecular weight cutoff 8000) at phosphate buffer solution (PBS) with 1 mg mL^{-1} HAase or without HAase. Briefly, drug–Fe_3O_4@mSiO₂–HA (30 mg) was dispersed in phosphate buffer solution A (PBS; 5 mL, pH 5.0, with HAase) and phosphate buffer solution B (PBS; 5 mL, pH 7.4, without HAase), respectively, and sealed in a dialysis bag, which was submerged in 50 mL of media solution at 37 °C with

gentle shaking. At interval time, the solution was taken out to determine the release amount by UV/Vis at 480/256 nm.

Cell culture

HeLa cells (cervical cancer cell line) were grown in monolayer in Dulbecco's Modified Eagle's Medium (DMEM, Gibco). MDA-MB-231 cells (breast cancer cell line), L02 human hepatocytes and HUVEC (human umbilical vein endothelial cell line) were grown in monolayer in RPMI-1640. They were all supplemented with 10% (v/v) fetal bovine serum (FBS, Tianhang bioreagent Co., Zhejiang) and penicillin/streptomycin (100 U mL^{-1} and 100 μg mL^{-1}, respectively, Gibco) in a humidified 5% CO_2 atmosphere at 37 °C.

Cell viability

The viability of cells in the presence of nanoparticles was investigated using an MTT (Sigma) assay. The assay was performed out in triplicate in the following manner. For MTT assay, all kinds of cells were seeded into 96-well plates at a density of 1×10^4 per well in 100 μL of media and grown overnight. The cells were then incubated with various concentrations of $Fe_3O_4@mSiO_2$, $Fe_3O_4@mSiO_2$–HA-2, DOX–$Fe_3O_4@mSiO_2$–HA-2, and Chl–$Fe_3O_4@mSiO_2$–HA-2 for 24 h. Following this incubation, cells were incubated in media containing 20 μL 5 mg mL^{-1} of MTT for 4 h. The media with MTT were removed, and 150 μL of DMSO was added to dissolve formazan crystal at room temperature for 30 min and the absorbance was measured at 490 nm by multi-detection microplate reader (SynergyTM HT, BioTek Instruments Inc., USA).

Confocal laser scanning microscopy (CLSM)

To check cellular uptake, HeLa cells were cultured in a 12-well chamber slide with one piece of cover glass at the bottom of each chamber in the incubation medium (DMEM) for 24 h. The cell nucleus was labeled by DAPI. DOX–$Fe_3O_4@mSiO_2$–HA-2 was added into the incubation medium at the concentration of 50 μg mL^{-1} for 0.5, 3, and 6 h incubation in 5% CO_2 at 37 °C. After the medium was removed, the cells were softly washed twice with PBS (pH 7.4) and the cover glass was visualized under a laser scanning confocal microscope (FluoView FV1000, Olympus).

Characterization

Transmission electron microscopy (TEM) images were recorded on TECNAI F20. Zeta potential and dynamic light scattering (DLS) was carried out with ZetaPALS Zeta Potential Annlyzer. The nitrogen adsorption/desorption, surface areas, and median pore diameter were measured using a Micromeritics ASAP 2010M sorptometer. Surface area was calculated according to the conventional BET method and the adsorption branches of the isotherms were used for the calculation of the pore parameters using the BJH method. Powder X-ray patterns (XRD) were recorded on a SIEMENSD 5005 X-ray diffractometer with Cu Kα radiation (40 kV, 30 mA). Fourier transform infrared (FTIR) spectra were recorded on a Perkin-Elmer 580B Infrared Spectrophotometer using the KBr pellet technique. A UV-vis spectrum was used to describe the amount of the drug release (SHIMADZU UV2550 spectrophotometer). The magnetic properties of samples were characterized with a Vibrating Sample Magnetometer (Lake Shore 7410). The photo-responsible treatment was carried out by a UV light source from Spot Light Curing, HSX-F300 (100 W, 350 nm).

Results and discussion

Morphology and structure

Fig. 1A shows the low-angle XRD patterns of $Fe_3O_4@mSiO_2$, DOX–$Fe_3O_4@mSiO_2$–HA-1, DOX–$Fe_3O_4@mSiO_2$–HA-2, and DOX–$Fe_3O_4@mSiO_2$–HA-3. As can be seen in Fig. 1A, all the samples reveal the diffraction peak at about $2\theta = 2.2°$, indicating their mesoporous structure. It is clearly observed that the relative diffraction intensities collected from DOX–$Fe_3O_4@mSiO_2$–HA-1, DOX–$Fe_3O_4@mSiO_2$–HA-2, and DOX–$Fe_3O_4@mSiO_2$–HA-3 reduces obviously compared to that of $Fe_3O_4@mSiO_2$ without drug loading and HA-gated. Besides, the more HA is covered on the $Fe_3O_4@mSiO_2$, the lower diffraction intensity the sample have, which is also in agreement with previous reports.[4] On the basis of the wide-angle XRD patterns of Fe_3O_4 and $Fe_3O_4@mSiO_2$ nanoparticles (Fig. 1B), all the diffraction peaks of Fe_3O_4 nanoparticles are in good agreement with that of standard Fe_3O_4 (JCPDS card no. 89-2355). The typical diffraction of Fe_3O_4 also can be found in the XRD pattern of $Fe_3O_4@mSiO_2$, thus attesting to the presence of Fe_3O_4. Moreover, an additional diffraction peak at 22.2° appears in $Fe_3O_4@mSiO_2$ due to the amorphous $mSiO_2$ structure.

Their morphologies and structures were further characterized through TEM analysis. Fig. 2 shows the typical TEM images of the nanocomposites. As displayed in Fig. 2A, it can be clearly seen that the Fe_3O_4 nanoparticles show the dispersed and uniform spheres with an average diameter about 20 nm. As revealed in Fig. 2B, the obvious core–shell structure with Fe_3O_4 core encapsulated by mesoporous silica shell was synthesized successfully. And the worm-like mesoporous structure of silica shell derived from the template CTAB agrees with the corresponding XRD pattern. The statistical average diameter of $Fe_3O_4@mSiO_2$ from TEM images was carried out by the Nano Measurer Soft (1.2). As displayed in Fig. S3,† the statistical average diameter of $Fe_3O_4@mSiO_2$ is 59.4 ± 2.42 nm. As present in Fig. S4,† there is not obvious difference on the morphology and average diameter of DOX–$Fe_3O_4@mSiO_2$–HA and $Fe_3O_4@mSiO_2$. However, it is believed that the blurry mesoporous structure and border of DOX–$Fe_3O_4@mSiO_2$–HA nanoparticles is ascribed to the HA coating.[44,45]

The pore structure and related textural properties of $Fe_3O_4@mSiO_2$, DOX–$Fe_3O_4@mSiO_2$–HA-1, DOX–$Fe_3O_4@mSiO_2$–HA-2, and DOX–$Fe_3O_4@mSiO_2$–HA-3 were investigated through nitrogen adsorption–desorption measurement. The corresponding adsorption isotherms and the pore diameter distribution curves are depicted in Fig. 3. From Fig. 3A, they display the typical IV adsorption isotherms with a steep capillary condensation steps at a relative pressure of $P/P_0 = 0.2$–0.4. The typical H4 hysteresis loop is observed, testifying the mesoporous structure of these samples. As can be seen in
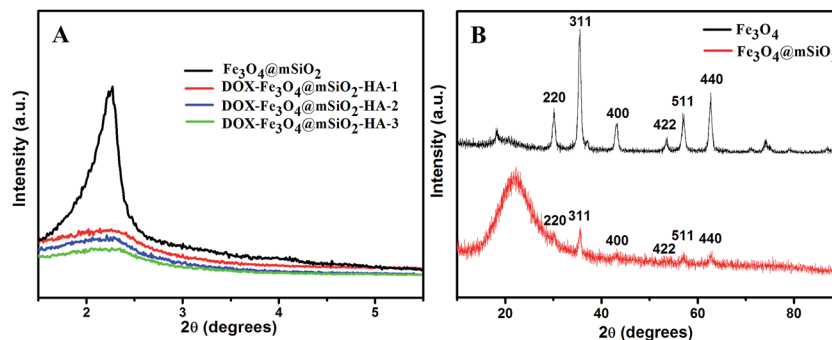
Fig. 1 (A) Low-angle XRD patterns of $Fe_3O_4@mSiO_2$, DOX–$Fe_3O_4@mSiO_2$–HA-1, DOX–$Fe_3O_4@mSiO_2$–HA-2, DOX–$Fe_3O_4@mSiO_2$–HA-3, and (B) wide-angle XRD patterns of Fe_3O_4 (black) and $Fe_3O_4@mSiO_2$ (red).
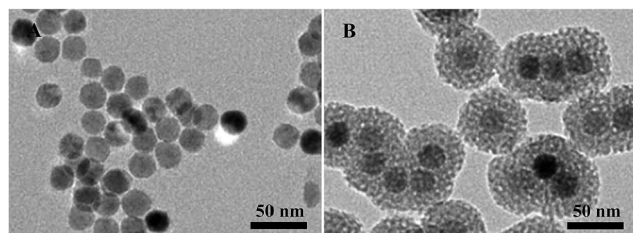
Fig. 2 TEM images of (A) Fe_3O_4, and (B) $Fe_3O_4@mSiO_2$.

Fig. 3A, the decreased uptakes amount of DOX–$Fe_3O_4@mSiO_2$–HAs, if taking its counterpart ($Fe_3O_4@mSiO_2$) as a comparison, could be found obviously. That also makes the surface area and pore volume reduced from 326 m^2 g^{-1} and 0.285 cm^3 g^{-1} of $Fe_3O_4@mSiO_2$ to 192 m^2 g^{-1} and 0.159 cm^3 g^{-1} of DOX–$Fe_3O_4@mSiO_2$–HA-1, 155 m^2 g^{-1} and 0.129 cm^3 g^{-1} of DOX–$Fe_3O_4@mSiO_2$–HA-2, 136 m^2 g^{-1} and 0.115 cm^3 g^{-1} of DOX–$Fe_3O_4@mSiO_2$–HA-3, respectively (Table 1). These decreased porous parameters demonstrate the HA coating and DOX molecules encapsulated in the $mSiO_2$ pores. Therefore, with the highest modifies of HA, DOX–$Fe_3O_4@mSiO_2$–HA-3 possesses the lowest surface area and pore volume (Table 1).

The FT-IR absorption measurement was carried out to characterize the functional modification of the system. The corresponding FT-IR spectra of $Fe_3O_4@mSiO_2$, $Fe_3O_4@mSiO_2$–NH_2, and $Fe_3O_4@mSiO_2$–HA are illustrated in Fig. 4. As shown in Fig. 4, the characteristic peaks of silica in the region around 1086 and 808 cm^{-1} that correspond to v_{as}(Si–O–Si) and v_s(Si–O–Si) can also be found in all the FT-IR spectra, testifying the SiO_2 framework of all samples. Other peaks at 2924 cm^{-1} are associated with the C–H stretching vibrations for organic components. Moreover, the deformation vibration bands of N–H at 1559 cm^{-1} also can be found in $Fe_3O_4@mSiO_2$–NH_2, testifying that –NH_2 groups have been successfully modified onto $Fe_3O_4@mSiO_2$. The two new peaks at 1635 (C=O stretching vibration of acid amide) and 1717 cm^{-1} (C=O deformation vibration of ester) appear, confirming that HA is coated on $Fe_3O_4@mSiO_2$–NH_2 successfully.

Additionally, the hydrodynamic diameter and corresponding zeta-potential of $Fe_3O_4@mSiO_2$, $Fe_3O_4@mSiO_2$–NH_2, m-HA,

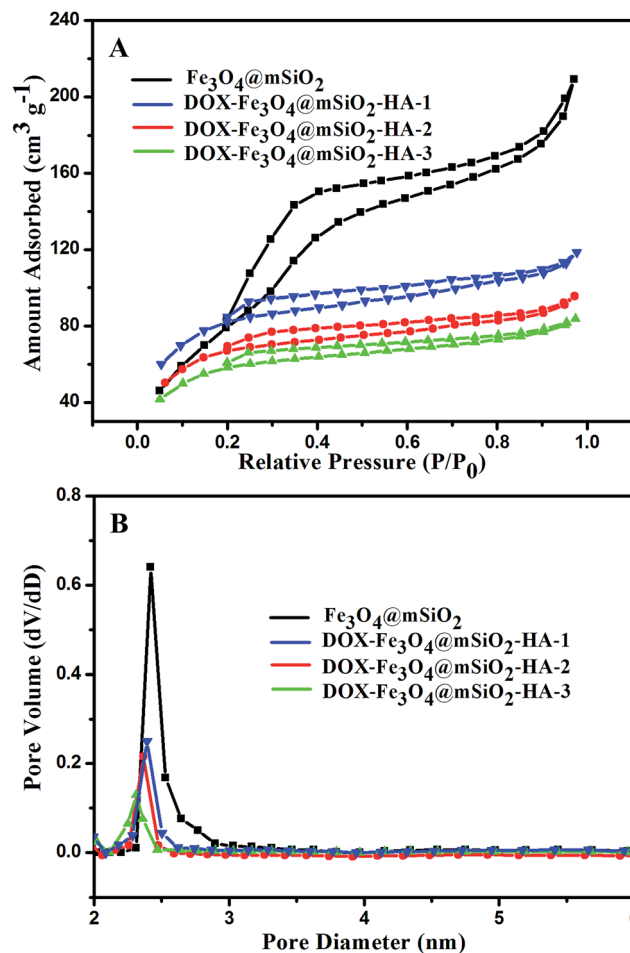**Fig. 3** (A) Nitrogen adsorption–desorption isotherms and (B) pore diameter distribution for $Fe_3O_4@mSiO_2$, DOX–$Fe_3O_4@mSiO_2$–HA-1, DOX–$Fe_3O_4@mSiO_2$–HA-2, and DOX–$Fe_3O_4@mSiO_2$–HA-3.

$Fe_3O_4@mSiO_2$–HA-1, $Fe_3O_4@mSiO_2$–HA-2, and $Fe_3O_4@mSiO_2$–HA-3 were measured to further illuminate the HA modification. As depicted in Fig. 5 and Table 2, $Fe_3O_4@mSiO_2$ exhibits an average diameter of about 82.0 nm and zeta potential of -15.01 ± 2.17 mV derived from the abundant surface Si–OH. Next, the –NH_2 was grafted onto the surface of $Fe_3O_4@mSiO_2$

Table 1 Pore parameters of the samples

Samples	Surface area ($m^2 g^{-1}$)	Pore volume ($cm^3 g^{-1}$)	Pore diameter (nm)
Fe_3O_4@mSiO_2	326	0.285	2.42
DOX–Fe_3O_4@mSiO_2–HA-1	192	0.159	2.39
DOX–Fe_3O_4@mSiO_2–HA-2	155	0.129	2.36
DOX–Fe_3O_4@mSiO_2–HA-3	136	0.115	2.31

via silane coupling reaction (APTES), which results in the increased particle diameter (85.4 nm) and zeta potential (64.19 ± 3.38 mV). Then, drug–Fe_3O_4@mSiO_2–NH_2 was added into a solution with the negatively charged HA modified with polymerizable acrylate groups (designated m-HA) (−52.24 ± 2.52) (Fig. S1, ESI†) and a crosslinker MBA, followed by the interfacial polymerization *via* UV irradiation to obtain drug–Fe_3O_4@ mSiO_2–HA. And the corresponding diameter and corresponding zeta-potential of these particles raise to 160.7 nm and −10.12 ± 2.21 mV (Fe_3O_4@mSiO_2–HA-1), 218.1 nm and −19.87 ± 2.72 mV (Fe_3O_4@mSiO_2–HA-2), 280.6 nm and −25.60 ± 1.91 mV (Fe_3O_4@mSiO_2–HA-3), respectively. Based on the above investigation, the notably increased particle diameter indicates the successful coating of the HA-crosslinked layer on the surface of Fe_3O_4@mSiO_2. And the highly negative surface charge, owing to the increase of the negative charge HA-crosslinked gel, further testifies the present of HA layer outside Fe_3O_4@mSiO_2 nanoparticles. Coated with most HA, Fe_3O_4@mSiO_2–HA-3 displays the largest diameter and lowest zeta potential of all.

The field dependence of magnetization characterization for the DOX–Fe_3O_4@mSiO_2–HA-1, DOX–Fe_3O_4@mSiO_2–HA-2, and DOX–Fe_3O_4@mSiO_2–HA-3 was measured using a VSM at room temperature. As shown in Fig. 6A, significant hysteresis loops indicate the super-paramagnetism of all materials. The saturation magnetizations (M_s) of DOX–Fe_3O_4@mSiO_2–HA-1, DOX–Fe_3O_4@mSiO_2–HA-2, and DOX–Fe_3O_4@mSiO_2–HA-3 are about 23.5, 18.0, and 10.6 emu g^{-1}, respectively, that is ascribed
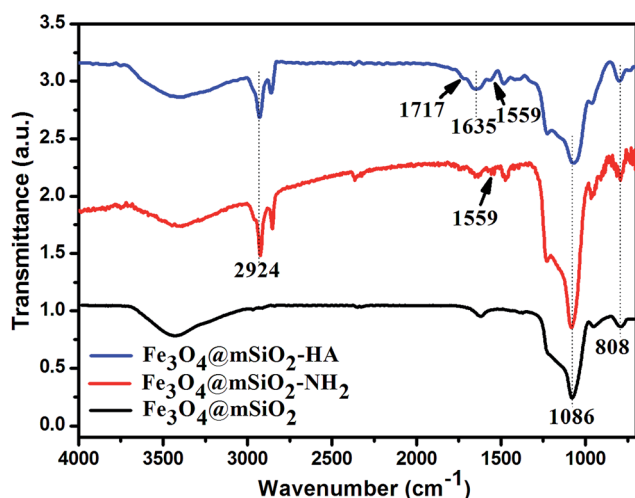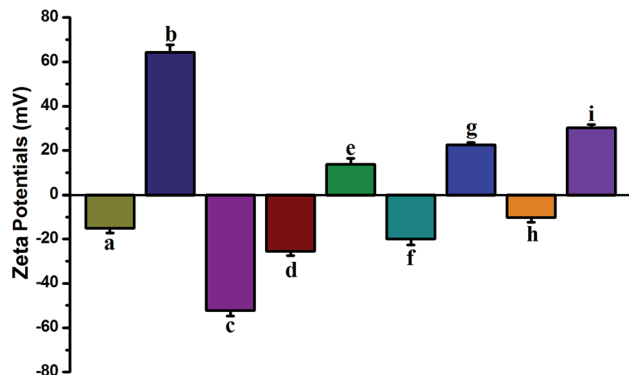
Fig. 5 Zeta-potential test of (a) Fe_3O_4@mSiO_2, (b) Fe_3O_4@mSiO_2–NH_2, (c) m-HA, (d) Fe_3O_4@mSiO_2–HA-3, (e) Fe_3O_4@mSiO_2–HA-3 incubated with HAase, (f) Fe_3O_4@mSiO_2–HA-2, (g) Fe_3O_4@mSiO_2–HA-2 incubated with HAase, (h) Fe_3O_4@mSiO_2–HA-1, (i) Fe_3O_4@mSiO_2–HA-1 incubated with HAase.

to the presence of nonmagnetic components, including mSiO_2, DOX, and HA. In addition, these nanoparticles exhibit good redispersibility and magnetic enrichment (inset), which suggests that they can be manipulated by an external magnetic field, thereby revealing its potential application for passive targeting on drug delivery.

Drug loading and release profiles

To investigate the enzyme sensitive release behaviors of DOX–Fe_3O_4@mSiO_2–HAs systems, DOX was firstly selected as the model drug to evaluate the loading and controlled release dynamics. The actual loading capacity is calculated to be 4.58 ± 0.5, 4.62 ± 0.3 and 4.80 ± 0.6 wt% for DOX–Fe_3O_4@mSiO_2–HA-1, DOX–Fe_3O_4@mSiO_2–HA-2, and DOX–Fe_3O_4@mSiO_2–HA-3 (based on formula (1)), respectively. The enzyme-sensitive drug release behaviors under stimulated tumor (HAase 1 mg mL^{-1} at pH 5.0) and normal tissue (without HAase at pH 7.4) environment were investigated by UV/Vis absorption spectroscopy. As can be seen in Fig. 7A, without HAase DOX–Fe_3O_4@-mSiO_2–HAs nanoparticles reveal just below 10% of DOX release within 48 h. In contrast, the presence of HAase accelerates the

Fig. 4 FTIR spectra of Fe_3O_4@mSiO_2, Fe_3O_4@mSiO_2–NH_2, and Fe_3O_4@mSiO_2–HA.

Table 2 Hydrodynamic size of the samples

Samples	Hydrodynamic size distribution (diameter, nm)
Fe_3O_4@mSiO_2	82.0
Fe_3O_4@mSiO_2–NH_2	85.4
Fe_3O_4@mSiO_2–HA-3	280.6
Fe_3O_4@mSiO_2–HA-2	218.1
Fe_3O_4@mSiO_2–HA-1	160.7
Fe_3O_4@mSiO_2–HA-3 incubated with HAase	122.4
Fe_3O_4@mSiO_2–HA-2 incubated with HAase	104.4
Fe_3O_4@mSiO_2–HA-1 incubated with HAase	98.1
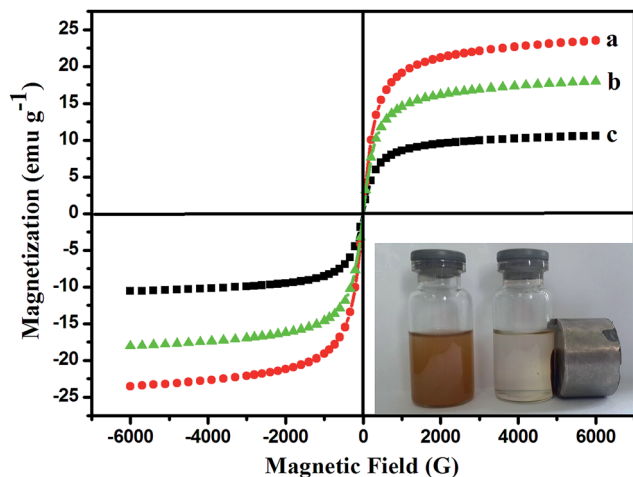
Fig. 6 Representative hysteresis-loop measurements of the obtained (a) DOX–Fe$_3$O$_4$@mSiO$_2$–HA-1, (b) DOX–Fe$_3$O$_4$@mSiO$_2$–HA-2, and (c) DOX–Fe$_3$O$_4$@mSiO$_2$–HA-3. Inset: the photograph of redispersibility and magnetic enrichment manipulated by an external magnet.

increasing the amount of HA causes the increased HA layer coating outside the nanocomposites. Coated with most HA, Fe$_3$O$_4$@mSiO$_2$–HA-3 displays the largest diameter (280.6 nm) and lowest zeta potential (-25.60 ± 1.91 mV) of all. Furthermore, the decreased surface area and pore volume (136 m^2 g^{-1} and 0.115 cm^3 g^{-1}) of DOX–Fe$_3$O$_4$@mSiO$_2$–HA-3 also derived from the thickest HA layer coating outside, making the lowest release amount as present in Fig. 7. So, coated with the least HA, Fe$_3$O$_4$@mSiO$_2$–HA-1 reveals the most release amount of all samples.

To further verify the enzyme-sensitive drug release, the release of DOX from DOX–Fe$_3$O$_4$@mSiO$_2$–HAs without HAase (pH 7.4) at the first 24 h and then with the addition of HAase (pH 5.0) was studied. As shown in Fig. 7B, DOX release slowly to reach 8.54% at the first 24 h, but the release is improved to 48.86% for the next 24 h, further illuminating the HAase triggered drug release. Another anti-cancer drug, Chl was adopted and the corresponding release curves were investigated in Fig. 7C and D. It is clearly observed that Chl–Fe$_3$O$_4$@mSiO$_2$–HAs also reveal the HAase enhanced release behaviors as DOX–Fe$_3$O$_4$@mSiO$_2$–HAs (Fig. 7A and B), and without HAase few Chl leakage can be detected. After the treatment with HAase, Chl–Fe$_3$O$_4$@mSiO$_2$–HA-1, Chl–Fe$_3$O$_4$@mSiO$_2$–HA-2, and Chl–Fe$_3$O$_4$@mSiO$_2$–HA-3 exhibit $99.48 \pm 2.56\%$, $88.49 \pm 3.38\%$, and $62.33 \pm 2.12\%$ drug release at 48 h.

From Fig. 7, it is proved that the drug molecules can be encapsulated in the mesopore by HA layer effectively to avoid
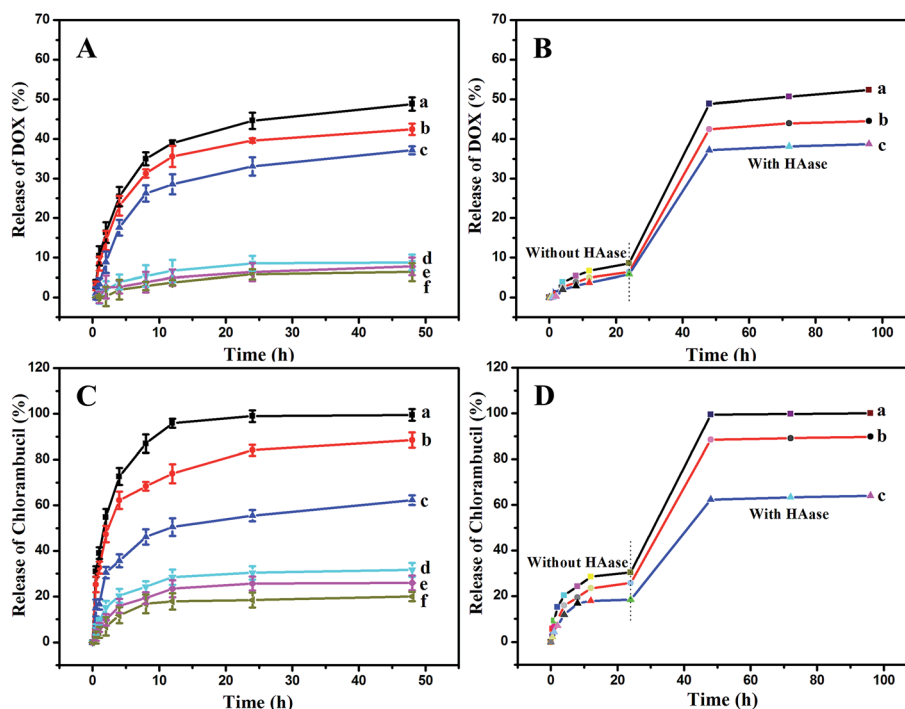
release of DOX from DOX–Fe$_3$O$_4$@mSiO$_2$–HAs, obviously. From Fig. 7A, it takes 48 h to reach the maximal amount $48.86 \pm 1.63\%$, $42.51 \pm 1.44\%$, and $37.18 \pm 1.01\%$ with HAase treatment for DOX–Fe$_3$O$_4$@mSiO$_2$–HA-1, DOX–Fe$_3$O$_4$@mSiO$_2$–HA-2, and DOX–Fe$_3$O$_4$@mSiO$_2$–HA-3, respectively. As shown in Table 2,

Fig. 7 (A) Release profiles under (a–c) stimulated tumor (HAase at pH 5.0) and (d–f) stimulated normal tissue (without HAase at pH 7.4) media of (■) DOX–Fe$_3$O$_4$@mSiO$_2$–HA-1, (●) DOX–Fe$_3$O$_4$@mSiO$_2$–HA-2, and (▲) DOX–Fe$_3$O$_4$@mSiO$_2$–HA-3; (B) cumulative release rates of DOX under the switched conditions: (a) DOX–Fe$_3$O$_4$@mSiO$_2$–HA-1, (b) DOX–Fe$_3$O$_4$@mSiO$_2$–HA-2, (c) DOX–Fe$_3$O$_4$@mSiO$_2$–HA-3; (C) release profiles under (a–c) stimulated tumor (HAase at pH 5.0) and (d–f) stimulated normal tissue (without HAase at pH 7.4) media of (■) Chl–Fe$_3$O$_4$@mSiO$_2$–HA-1, (●) Chl–Fe$_3$O$_4$@mSiO$_2$–HA-2, and (▲) Chl–Fe$_3$O$_4$@mSiO$_2$–HA-3; (D) cumulative release rates of Chl under the switched conditions: (a) Chl–Fe$_3$O$_4$@mSiO$_2$–HA-1, (b) Chl–Fe$_3$O$_4$@mSiO$_2$–HA-2, (c) Chl–Fe$_3$O$_4$@mSiO$_2$–HA-3.
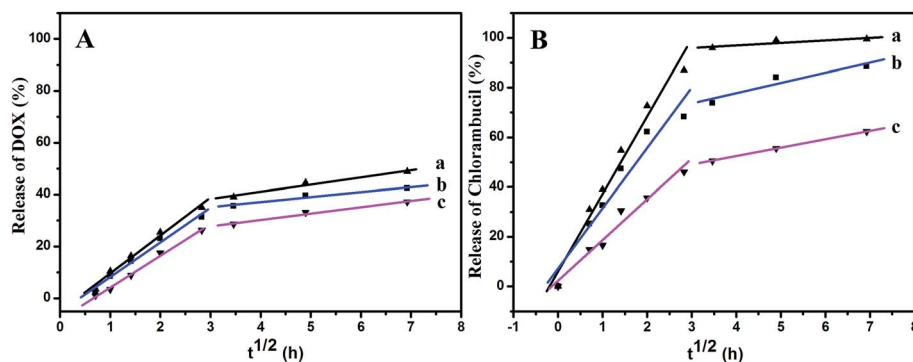
Fig. 8 (A) Higuchi plot for the release of DOX from DOX–Fe$_3$O$_4$@mSiO$_2$–HAs with HAase (pH 5.0), (a) DOX–Fe$_3$O$_4$@mSiO$_2$–HA-1, (b) DOX–Fe$_3$O$_4$@mSiO$_2$–HA-2, (c) DOX–Fe$_3$O$_4$@mSiO$_2$–HA-3; (B) Higuchi plot for the release of Chl from Chl–Fe$_3$O$_4$@mSiO$_2$–HAs with HAase (pH 5.0), (a) Chl–Fe$_3$O$_4$@mSiO$_2$–HA-1, (b) Chl–Fe$_3$O$_4$@mSiO$_2$–HA-2, (c) Chl–Fe$_3$O$_4$@mSiO$_2$–HA-3.

premature release and reduce the side effects. The novel selective release is ascribed to the activity of the "HA gate", which is sensitive to some reducing agents, such as HAase, and it is degradable to cause the "gate" open and drug release. Without HAase, HA shell still encapsulates the cargo within the pores to void drug leakage. In addition, HAase is the major enzyme found in the tumor microenvironment.[46,47] So, HA layer could be readily degraded into low molecular weight fragments after these drug–Fe$_3$O$_4$@mSiO$_2$–HA nanoparticles being endocytosed by cancer cells. These significant performances give rise to the potential application of the drug–Fe$_3$O$_4$@mSiO$_2$–HA systems on tumor treatment. The possible sensitive mechanism was studied by the analysis of the hydrodynamic diameter and zeta-

potential of Fe$_3$O$_4$@mSiO$_2$–HA-1, Fe$_3$O$_4$@mSiO$_2$–HA-2, and Fe$_3$O$_4$@mSiO$_2$–HA-3 after treating with HAase. From Fig. 5 and Table 2, the hydrodynamic diameter reduced to 98.1 (Fe$_3$O$_4$@mSiO$_2$–HA-1), 104.4 (Fe$_3$O$_4$@mSiO$_2$–HA-2), and 122.4 nm (Fe$_3$O$_4$@mSiO$_2$–HA-3). Furthermore, the zeta-potential also increases to 30.26 ± 1.54 (Fe$_3$O$_4$@mSiO$_2$–HA-1), 22.52 ± 1.08 (Fe$_3$O$_4$@mSiO$_2$–HA-2), and 13.78 ± 2.71 mV (Fe$_3$O$_4$@mSiO$_2$–HA-3). Based the above investigation, it is confirmed that the decreased hydrodynamic diameter and increased zeta-potential can be ascribed to the HAase, and the triggered release is caused by the sensitive degradation of HA shell by HAase.

To further investigate the release behavior, the release data were analyzed by using the Higuchi model.[48,49] As we known,
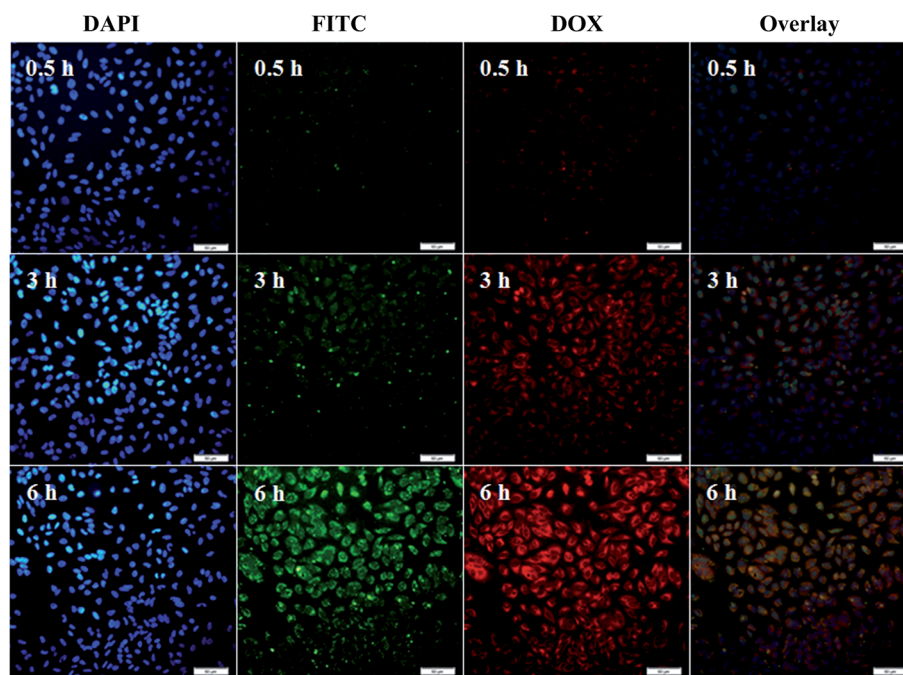

Fig. 9 Confocal laser scanning microscopy (CLSM) images of HeLa cells incubated with DOX–Fe$_3$O$_4$@mSiO$_2$–HA-2 for 0.5, 3, and 6 h at 37 °C. DAPI labeled cells nucleus (blue), DOX fluorescence in cells (red), FITC labeled DOX–Fe$_3$O$_4$@mSiO$_2$–HA-2 (green), and overlay. Scale bars for all images are 50 μm.
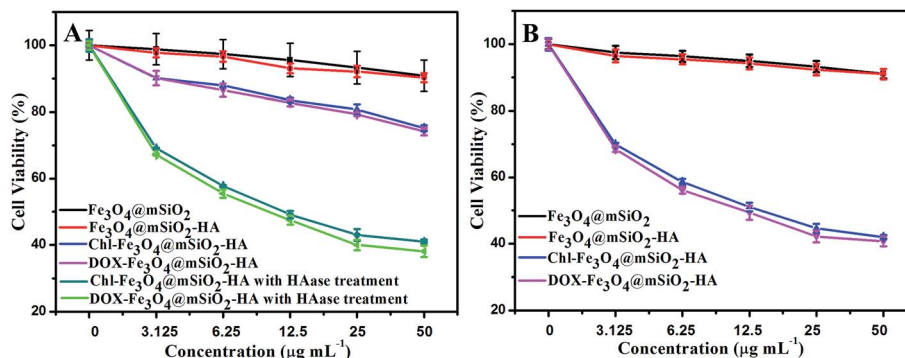
Fig. 10 *In vitro* cell viability incubated with different amounts of $Fe_3O_4@mSiO_2$, $Fe_3O_4@mSiO_2$–HA-2, DOX–$Fe_3O_4@mSiO_2$–HA-2, and Chl–$Fe_3O_4@mSiO_2$–HA-2 (A) without HAase or with HAase treatment toward HeLa cells for 24 h; (B) toward MDA-MB-231 cells for 24 h.

drug release kinetics from an insoluble, porous carrier matrix are frequently described by the Higuchi model, and the release rate can be described by the follow eqn (2):

$$Q = k \times t^{1/2} \qquad (2)$$

in which Q is the quantity of drug released from the materials, t denotes time, and k is the Higuchi dissolution constant. According to the model, for a purely diffusion-controlled process, the linear relationship is valid for the release of relatively small molecules distributed uniformly throughout the carrier.[50]

As illustrated in Fig. 8, all release curves with HAase displays the special two-step release performance with a good line relationship based on the Higuchi model. From Fig. 8A, DOX–$Fe_3O_4@mSiO_2$–HAs exhibit the two-step release (0–8 h and 8–48 h) and dissolution constant k (the slope of the fitting line) of the first step is higher than that of the second step. Besides that, with lowest amount of HA shell, DOX–$Fe_3O_4@mSiO_2$–HA-1 possesses the highest dissolution constant k (in the first 8 h), followed with DOX–$Fe_3O_4@mSiO_2$–HA-2 and DOX–$Fe_3O_4@mSiO_2$–HA-3. That is because with the lowest amount of HA, the HA shell could be degraded fastest, making the highest dissolution constant k as well as the fastest release amount of DOX–$Fe_3O_4@mSiO_2$–HA-1. In the second release step (8–48 h), all the dissolution constants decrease obviously and tend to similar to each other. As shown in Fig. 8, most drug molecules release outside with the collapse of "gatekeeper" in the first release step. It is believed that the first release step depends mainly upon the degradation of HA and the second release step is determined just by the mesoporous structure of the host. From Fig. 8B, Chl–$Fe_3O_4@mSiO_2$–HAs displays the larger dissolution constant and release amount than DOX–$Fe_3O_4@mSiO_2$–HAs. It is known that, DOX is a typical of positive charge drug, which possesses the strong static interaction with HA layer (negative), so that it is difficult for DOX–$Fe_3O_4@mSiO_2$–HAs to exhibit the high release amount (up to 48.86%, with HAase). However, Chl is a typical negative charge drug. The repulsive force between negative Chl and negative HA layer leads to the free release through the HA fragment as well as the higher dissolution constant and release amount (up to 99.48%, with HAase). To sum up, the amount of "gate" (HA) associating with the

interaction between the drug molecules and "gate" (HA) can regulate the release performance of the system.

In vitro cytotoxic effect and cellular uptake

To investigate the cellular uptake process of the sample, the cellular uptake and subsequent localization was studied. Fig. 9 shows the CLSM images of HeLa cells incubated with DOX–$Fe_3O_4@mSiO_2$–HA-2 for 0.5, 3, and 6 h. The blue fluorescence is from DAPI used to mark the nuclei, the red emission originates from the loaded DOX, and the green color derives from fluorescein isothiocyanate (FITC) of the nanoparticles, which is used to track the carrier. In the first 0.5 h, there is little red emission and green fluorescence, revealing only a few DOX–$Fe_3O_4@mSiO_2$–HA-2 nanoparticles has been taken up by HeLa cells. After the incubation for 3 h, the obvious green and red fluorescence emission of DOX–$Fe_3O_4@mSiO_2$–HA-2 is observed in the cytoplasm, suggesting that more particles are localized in the cells. Further increase the incubation time, the red and green colour in cell becomes stronger and stronger. The fast cellular uptake ability of the sample is ascribing to the small particle size that benefits to enter into the cells and enhances the drug efficacy.[51–53]

The investigation of the cytotoxicity of the synthesized drug carriers is significant for its potential biomedical applications. Only nontoxic carriers are suitable for bio-pharmaceuticals study. At first, the *in vitro* cytotoxicity of $Fe_3O_4@mSiO_2$, $Fe_3O_4@mSiO_2$–HA-2, DOX–$Fe_3O_4@mSiO_2$–HA-2, and Chl–$Fe_3O_4@mSiO_2$–HA-2 against two different kinds of cancer cells (HeLa and MDA-MB-231 cells) and two different kinds of normal cells (L02 human hepatocytes and HUVEC) was evaluated by means of a standard MTT cell assay (Fig. 10 and S5†). It could be seen that both $Fe_3O_4@mSiO_2$ and $Fe_3O_4@mSiO_2$–HA-2 show ignored cytotoxic effect on the four different kinds of cells in a range of concentration (3.125–50 $\mu g\ mL^{-1}$). As can be seen in Fig. 10 and S5,† the cell viability of $Fe_3O_4@mSiO_2$–HA-2 attains $90.30 \pm 1.35\%$, $90.99 \pm 1.54\%$, $91.66 \pm 1.19\%$, and $93.35 \pm 1.25\%$ for HeLa, MDA-MB-231, L02 human hepatocytes and HUVEC, respectively, even its concentration reaches 50 $\mu g\ mL^{-1}$, suggesting their benign biocompatibility. This encouraging result stimulates us to perform the MTT tests towards the

drug–Fe$_3$O$_4$@mSiO$_2$–HA. It can be seen that even after incubation with DOX–Fe$_3$O$_4$@mSiO$_2$–HA-2 and Chl–Fe$_3$O$_4$@mSiO$_2$–HA-2 for 24 h at a concentration of 50 µg mL^{-1}, L02 human hepatocytes and HUVEC can keep as high as 83.56 ± 3.12% and 85.54 ± 2.31%, 84.56 ± 3.76% and 86.54 ± 2.42%, respectively. So, we can conclude that the prepared drug delivery system of this work possesses good, at least comparable, biocompatibility compared with widely reported drug delivery systems. After the drug-loading, DOX–Fe$_3$O$_4$@mSiO$_2$–HA-2 and Chl–Fe$_3$O$_4$@mSiO$_2$–HA-2 (50 µg mL^{-1}, after HAase treatment) display a significantly promoted cytotoxicity (61.88 ± 1.75% and 58.97 ± 0.60%) against HeLa cells. Based on the above investigate, with the treatment of enzyme (HAase), the anti-cancer drug can break away from these composites to induce the decreased cell viability. However, without the HAase treatment, the cell viability of DOX–Fe$_3$O$_4$@mSiO$_2$–HA-2 and Chl–Fe$_3$O$_4$@mSiO$_2$–HA-2 (50 µg mL^{-1}) also retain 74.21 ± 1.16% and 75.16 ± 0.94%.

To demonstrate the enzyme-triggered drug release further, we selected the MDA-MB-231 cells (breast cancer cells) which have the CD44 receptor as the intracellular HAase cells. And HA could be readily degraded by lysosomal enzyme HAase, which is the major enzyme found in their microenvironment, into low molecular weight fragments after being endocytosed by MDA-MB-231 cells.[44,54] The cell viability of DOX–Fe$_3$O$_4$@mSiO$_2$–HA-2 and Chl–Fe$_3$O$_4$@mSiO$_2$–HA-2 at 50 µg mL^{-1} after 24 h are 40.75 ± 1.55% and 42.03 ± 0.60% for MDA-MB-231 cells, respectively, indicating the good performance of the designed enzyme-triggered drug release systems (Fig. 10B). Consequently, with sound bioactivity, fast uptake, and the enzyme triggered drug release, drug–Fe$_3$O$_4$@mSiO$_2$–HA can be regarded as a promising candidate in biomedicine.

Conclusions

In summary, Fe$_3$O$_4$@mSiO$_2$ nanomaterials with a statistical average diameter of 59.4 ± 2.42 nm were successfully synthesized as the host, followed by attaching HA cross-linked gel shell *via situ* polymerization method. The drug–Fe$_3$O$_4$@mSiO$_2$–HA revealed the enzyme triggered drug release kinetics, owing to the degradation of HA shell by HAase. And the amount of HA shell associating with the interaction between the drug molecules and HA can determine the release performance of the system. Moreover, a series of the cell experiments were carried out to further reveal the fast cell uptake and the superior enzyme-sensitive drug release. And the HA receptors and overexpressed HAase in many tumor microenvironment induce the specific targeting enrichment and drug release that combines the magnetic target insure their potential application on tumor therapy.

Acknowledgements

References

1 C. Li, M. F. Penet, F. Wildes, T. Takagi, Z. H. Chen, P. T. Winnard, J. D. Artemov and Z. M. Bhujwalla, *ACS Nano*, 2010, **4**, 6707–6716.

2 A. A. Zaki, D. Joh, Z. L. Cheng, A. L. B. D. Barros, G. Kao, J. Dorsey and A. Tsourkas, *ACS Nano*, 2014, **8**, 104–112.

3 L. E. Kelderhouse, V. Chelvam, C. Wayua, S. Mahalingam, S. Poh, S. A. Kularatne and P. S. Low, *Bioconjugate Chem.*, 2013, **24**, 1075–1080.

4 C. Y. Yang, W. Guo, L. R. Cui, N. An, T. Zhang, G. Guo, H. M. Lin and F. Y. Qu, *J. Mater. Chem. B*, 2015, **3**, 1010–1019.

5 R. C. Lv, P. P. Yang, F. He, S. L. Gai, G. X. Yang and J. Lin, *Chem. Mater.*, 2015, **27**, 483–496.

6 D. M. Yang, P. A. Ma, Z. Y. Hou, Z. Y. Cheng, C. X. Li and J. Li, *Chem. Soc. Rev.*, 2015, **44**, 1416–1448.

7 A. Singh, M. Talekar, T. H. Tran, A. Samanta, R. Sundaram and M. Amiji, *J. Mater. Chem. B*, 2014, **2**, 8069–8084.

8 Q. Y. Hu, P. S. Katti and Z. Gu, *Nanoscale*, 2014, **6**, 12273–12286.

9 N. Larson and H. Ghandehari, *Chem. Mater.*, 2012, **24**, 840–853.

10 P. P. Yang, S. L. Gai and J. Lin, *Chem. Soc. Rev.*, 2012, **41**, 3679–3698.

11 A. Popat, S. B. Hartono, F. Stahr, J. Liu, S. Z. Qiao and G. Q. Lu, *Nanoscale*, 2011, **3**, 2801–2818.

12 D. Tarn, C. E. Ashley, M. Xue, E. C. Carnes, J. I. Zink and C. J. Brinker, *Acc. Chem. Res.*, 2013, **46**, 792–801.

13 H. Kim, S. Kim, C. Y. Park, H. Lee, H. J. Park and C. Kim, *Adv. Mater.*, 2010, **22**, 4280–4283.

14 Y. N. Zhao, B. G. Trewyn, I. I. Slowing and V. S. Y. Lin, *J. Am. Chem. Soc.*, 2009, **131**, 8398–8400.

15 R. M. Li, L. Li, Y. H. Han, S. L. Gai, F. He and P. P. Yang, *J. Mater. Chem. B*, 2014, **2**, 2127–2135.

16 M. F. Shao, F. Y. Ning, J. W. Zhao, M. Wei, D. G. Evans and X. Duan, *J. Am. Chem. Soc.*, 2012, **134**, 1071–1077.

17 W. P. Li, P. Y. Liao, C. H. Su and C. S. Yeh, *J. Am. Chem. Soc.*, 2014, **136**, 10062–10075.

18 C. R. Thomas, D. P. Ferris, J. H. Lee, E. Choi, M. H. Cho, E. S. Kim, J. F. Stoddart, J. S. Shin, J. Cheon and J. I. Zink, *J. Am. Chem. Soc.*, 2010, **132**, 10623–10625.

19 W. Guo, C. Y. Yang, H. M. Lin and F. Y. Qu, *Dalton Trans.*, 2014, **43**, 18056–18065.

20 R. Casasús, M. D. Marcos, R. Martínez-Máñez, J. V. Ros-Lis, J. Soto, L. A. Villaescusa, P. Amorós, D. Beltrán, C. Guillem and J. Latorre, *J. Am. Chem. Soc.*, 2004, **126**, 8612–8613.

21 Y. R. Zheng, K. Suntharalingam, T. C. Johnstone, H. Yoo, W. Lin, J. G. Brooks and S. J. Lippard, *J. Am. Chem. Soc.*, 2014, **136**, 8790–8798.

22 R. S. Sørensen, A. H. Okholm, D. Schaffert, A. L. B. Kodal, K. V. Gothelf and J. Kjems, *ACS Nano*, 2013, **7**, 8098–8104.

23 C. Y. Yang, W. Guo, L. R. Cui, N. An, T. Zhang, H. M. Lin and F. Y. Qu, *Langmuir*, 2014, **30**, 9819–9827.

24 Y. L. Zhao, Z. Li, S. Kabehie, Y. Y. Botros, J. F. Stoddart and J. I. Zink, *J. Am. Chem. Soc.*, 2010, **132**, 13016–13025.

25 X. Zhang, X. W. Xu, T. T. Li, M. Lin, X. Y. Lin, H. Zhang, H. C. Sun and B. Yang, *ACS Appl. Mater. Interfaces*, 2014, **6**, 14552–14561.

26 G. Liu, J. H. Gao, H. Ai and X. Y. Chen, *Small*, 2013, **9**, 1533–1545.

27 R. Hao, R. J. Xing, Z. C. Xu, Y. L. Hou, S. Gao and S. H. Sun, *Adv. Mater.*, 2010, **22**, 2729–2742.

28 G. H. Qin, Z. W. Fang and C. Y. Wang, *Dalton Trans.*, 2015, **44**, 5735–5745.

29 S. I. Stoeva, F. W. Huo, J. S. Lee and C. A. Mirkin, *J. Am. Chem. Soc.*, 2005, **127**, 15362–15363.

30 H. J. Qiu, B. Cui, G. M. Li, J. H. Yang, H. X. Peng, Y. S. Wang, N. N. Li, R. C. Gao, Z. G. Chang and Y. Y. Wang, *J. Phys. Chem. C*, 2014, **118**, 14929–14937.

31 Y. Chen, H. R. Chen, D. P. Zeng, Y. B. Tian, F. Chen, J. W. Feng and J. L. Shi, *ACS Nano*, 2010, **4**, 6001–6013.

32 Z. W. Chen, Z. H. Li, Y. H. Lin, M. L. Yin, J. S. Ren and X. G. Qu, *Chem.–Eur. J.*, 2013, **19**, 1778–1783.

33 M. Ma, H. R. Chen, Y. Chen, K. Zhang, X. Wang, X. Z. Cui and J. L. Shi, *J. Mater. Chem.*, 2012, **22**, 5615–5621.

34 M. H. Yu, S. Jambhrunkar, P. Thorn, J. Z. Chen, W. Y. Gu and C. Z. Yu, *Nanoscale*, 2013, **5**, 178–183.

35 L. W. Zhang, S. Gao, F. Zhang, K. Yang, Q. J. Ma and L. Zhu, *ACS Nano*, 2014, **8**, 12250–12258.

36 T. Y. Jiang, R. Mo, A. Bellotti, J. P. Zhou and Z. Gu, *Adv. Funct. Mater.*, 2014, **24**, 2295–2304.

37 P. Bertrand, N. Girard, C. Duval, J. Anjou, C. Chauzy, J. F. Ménard and B. Delpech, *Int. J. Cancer*, 1997, **73**, 327–331.

38 H. S. S. Qhattal and X. L. Liu, *Mol. Pharm.*, 2011, **8**, 1233–1246.

39 M. Bostad, M. Kausberg, A. Weyergang, C. E. Olsen, K. Berg, A. Høgset and P. K. Selbo, *Mol. Pharm.*, 2014, **11**, 2764–2776.

40 R. Mo, T. Y. Jiang, R. DiSanto, W. Y. Tai and Z. Gu, *Nat. Commun.*, 2014, **5**, 3364–3373.

41 J. Park, K. An, Y. H. Wang, J. G. Park, H. J. Noh, J. Y. Kim and T. Hyeon, *Nat. Mater.*, 2004, **3**, 891–895.

42 F. Muhammad, M. Y. Guo, W. X. Qi, F. X. Sun, A. F. Wang, Y. J. Guo and G. S. Zhu, *J. Am. Chem. Soc.*, 2011, **133**, 8778–8781.

43 E. Hachet, H. V. D. Berghe, E. Bayma, M. Block and R. A. Velty, *Biomacromolecules*, 2012, **13**, 1818–1827.

44 Z. W. Chen, Z. H. Li, Y. H. Lin, M. L. Yin, J. S. Ren and X. G. Qu, *Chem.–Eur. J.*, 2013, **19**, 1778–1783.

45 M. Ma, H. R. Chen, Y. Chen, K. Zhang, X. Wang, X. Z. Cui and J. L. Shi, *J. Mater. Chem.*, 2012, **22**, 5615–5621.

46 B. P. Toole, *Nat. Rev. Cancer*, 2004, **4**, 528–539.

47 R. Stern and M. J. Jedrzejas, *Chem. Rev.*, 2006, **106**, 818–839.

48 P. Nadrah, U. Maver, A. Jemec, T. Tišler, M. Bele, G. Dražić, M. Benčina, A. Pintar, O. Planinšek and M. Gaberšček, *ACS Appl. Mater. Interfaces*, 2013, **5**, 3908–3915.

49 W. Guo, C. Y. Yang, L. R. Cui, H. M. Lin and F. Y. Qu, *Langmuir*, 2014, **30**, 243–249.

50 J. Higuchi, K. Hayashi, M. Yagi and H. Kondo, *J. Phys. Chem. A*, 2002, **106**, 8609–8618.

51 X. Y. Yuan, D. C. Marcano, C. S. Shin, X. Hua, L. C. Isenhart, S. C. Pflugfelder and G. Acharya, *ACS Nano*, 2015, **9**, 1749–1758.

52 K. E. Fischer, A. Jayagopal, G. Nagaraj, R. H. Daniels, E. M. Li, M. T. Silvestrini and T. A. Desai, *Nano Lett.*, 2011, **11**, 1076–1081.

53 Q. J. He and J. L. Shi, *Adv. Mater.*, 2014, **26**, 391–411.

54 R. Mo, T. Y. Jiang, R. DiSanto, W. Y. Tai and Z. Gu, *Nat. Commun.*, 2014, **5**, 3364–3373.